Vacuum 220 (2024) 112806

Contents lists available at ScienceDirect

Vacuum

journal homepage: www.elsevier.com/locate/vacuum

Gallium phosphide conformal film growth on *in-situ* tri-TBP dry-cleaned InGaP/GaAs using atomic hydrogen ALD

SeongUk Yun [a], Ping-Che Lee [b], Cheng-Hsuan Kuo [b], Aaron J. Mcleod [a], Zichen Zhang [b], Victor Wang [b], James Huang [b], Harshil Kashyap [b], Charles H. Winter [c], Andrew C. Kummel [a,*]

[a] *Department of Chemistry and Biochemistry, University of California, San Diego, La Jolla, CA, 92093, United States*
[b] *Materials Science and Engineering Program, University of California, San Diego, La Jolla, CA, 92093, United States*
[c] *Department of Chemistry, Wayne State University, Detroit, MI, 48202, United States*

ARTICLE INFO

Handling Editor: Prof. L.G. Hultman

Keywords:
Indium gallium phosphide
Local epitaxy growth
Atomic H ALD
tri-TBP
Particle-free interface
Dry-clean

ABSTRACT

Nearly stoichiometric (high P/Ga ratio and low oxygen content) ~ 20 nm GaP epi-layers were conformally deposited on the side-walls of InGaP layers using an atomic H ALD process with triethyl gallium (TEGa) and tri-tertiary butyl phosphine (tri-TBP). The key for uniform nucleation is an *in-situ* tri-TBP dry-clean in 40 mTorr Ar and 160 mTorr H_2 without acidic wet-clean to generate a particle-free and damage-free InGaP surface which induces local epitaxy growth of homogeneous GaP thin films. The *in-situ* tri-TBP dry-clean removed the native oxide of InGaP, surface particles, and the residual impurities simultaneously. It is hypothesized that the key to the process is *in-situ* formation of $PH_x(C_4H_9)_y$ surface adsorbates from atomic H and tri-TBP surface reactions. *In-situ* AES, cross-sectional STEM image, *ex-situ* XPS, AFM, and EDS confirmed the formation of high-quality GaP thin films on InGaP/GaAs with a high-quality interface and smooth surface morphology.

1. Introduction

III-V semiconductor heterostructures have gained significant interest in optoelectronics due to their high refractive index and low band-gap [1,2]. The typical metal-organic chemical vapor deposition (MOCVD) epitaxy growth of III-V semiconductors is commercially enabling wafer production. However, there are several challenges of MOCVD at high temperatures for application to scaled optoelectronic devices and high aspect ratio structures such as side-wall, trench, and mesa; for these applications, uniformity, conformal deposition, atomic level control of thickness, and low-temperature deposition are critical [3]. Previous reports on the temperature dependence of InGaP growth on GaAs showed that reduced optical quality (photoluminescence (PL) intensity and FWHM) was observed at 500 °C substrate temperature as compared to 460 °C substrate temperature [4]. Therefore, it is desirable to develop low-temperature growth using the atomic layer deposition (ALD) process for the scaled optoelectronic devices with high aspect ratio structures.

Integrated III-V semiconductor devices are typically fabricated using sophisticated processes with inductively coupled plasma (ICP) for reactive-ion etching and consequent patterning [5,6]. The etching processes inevitably generate undesirable impurities and surface particles. Furthermore, the III-V materials form poor-quality native oxides when they are exposed to an oxygen-containing ambient [5,6]. The III-V quantum-well (QW) side-wall surfaces are easily oxidized after the mesa formation since exposure to an oxygen-containing environment is inevitable. This poor-quality native oxide and surface particles on the side-walls of the optoelectronic mesa devices are the biggest sources of non-radiative recombination, poor power efficiency, and leakage current [7]. Aluminum oxide and silicon oxide passivation are typically deposited in industrial semiconductor applications by ALD or plasma-enhanced chemical vapor deposition (PE-CVD) [8]. However, the metal oxide and SiO_2 deposition processes can promote the formation of thin amorphous III-V native oxide and a high density of disordered interfacial impurities. Gallium phosphide (GaP) could be a promising passivation layer for III-V semiconductors since it has an indirect band gap of 2.26 eV, a higher refractive index than most III-V semiconductors, and a small lattice mismatch with III-V semiconductors [1]. Han et al. reported that thin GaP layers and ~50 nm $In_{0.49}Ga_{0.51}P$ layers showed improved optical properties for InP quantum dots despite a small lattice mismatch (~4 %) between GaP and InGaP [9]. In addition to being a passivation layer, the GaP layer could

---

* Corresponding author.
E-mail address: akummel@ucsd.edu (A.C. Kummel).

https://doi.org/10.1016/j.vacuum.2023.112806
Received 14 June 2023; Received in revised form 18 September 2023; Accepted 16 November 2023

be a good buffer layer and hetero-junction layer for III-V semiconductor materials. Xue et al. reported that the band alignment of $In_xGa_{1-x}P$ compounds in the stable zinc blende structures changed smoothly with composition and InGaP could be electron-hole donor or acceptor [10].

Various thin film deposition processes have been studied for GaP growth; molecular beam epitaxy (MBE), metal-organic chemical vapor deposition (MOCVD), hydride vapor phase epitaxy, and plasma-enhanced atomic layer deposition (PE-ALD) at high temperatures (≥600 °C) [11–17]. Applying a plasma source to epitaxy growth for ion bombardment (Ar^+, atomic H, or NH_4^+) could lower the process temperature and enable to use of the precursor with low reactivity for epitaxial III–V semiconductors [18,19]. Gudovskihk et al. reported the growth of microcrystalline GaP on Si at low temperature (~380 °C) by using a continuous atomic H plasma with PH_3 and TMGa [20]. Uvarov et al. recently showed the local epitaxy growth of GaP thin layers on Si using PE-ALD (additional Ar plasma pulse) with PH_3 and TMGa at temperatures below 400 °C [21]. Recently, crystallized GaP was successfully deposited on a Si substrate using atomic H ALD for the formation of highly ordered GaP using a tri-TBP dry-clean method for homogeneous nucleation [22]. However, the conformal deposition of crystallized GaP thin films has not been widely studied using a low-temperature ALD process on flat InGaP substrates or mesa side-walls of InGaP layers.

Atomic hydrogen dry-clean pre-treatment for III-V semiconductors has been studied for the removal of native oxide, formation of high-quality interfaces, and pre-treatment for ALD processes. Yamada et al. reported that atomic H could reduce the Ga_2O_3 on GaAs substrate to Ga_2O, leading to the desorption of Ga-oxide above 400 °C [23]. Weiss et al. demonstrated that molecular H_2 could lower the deoxidation onset temperature of In_2O_3 or Ga_2O_3 on InSb and GaSb by ~100 °C to volatile In_2O at 250 °C and Ga_2O at 400–470 °C [24]. The Ga_2O species could be evaporated even below 400 °C with the presence of plasma stimulation [25,26]. Bell et al. reported that atomic H decreased O and C impurities on InAs, GaSb, and InSb without loss of surface stoichiometry, but still relatively high O content (~10 at.%), ~3 μm In droplets, and III-V metallic clusters were observed on the surface after atomic H dry-clean. The trimethylaluminum (TMA) only process after atomic H dry-clean was proposed for the formation of a high-*k* Al_2O_3 interface layer instead of native oxide on GaAs substrate [27,28]. However, the impact of the TMA process on phosphide substrates (GaP and InGaP) has not been studied and the present oxide-free tri-TBP (tri-*tert*-butylphosphine) plus atomic H process might be promising to apply for the entire phosphide ALD process.

The impact of *in-situ* tri-TBP dry-clean pre-treatment (tri-TBP + atomic H) on the native oxide and surface particles of InGaP/GaAs substrate as a function of dry-clean time and the chamber pressure is reported in the present study. The ALD technique in the present study is denoted as the atomic H ALD since the plasma process employed atomic H as an individual pulse in each ALD cycle. The GaP atomic H ALD process was investigated for the formation of high P/Ga atomic ratio and low oxygen content GaP films by tuning the process temperature. Local epitaxy growth of crystallized GaP thin films were successfully achieved on the side-walls of InGaP layer using *in-situ* tri-TBP dry-clean and GaP atomic H ALD process; the interfacial layer was free of particles, oxides, and impurities. This is the first report of low-temperature growth of high-quality GaP thin films by ALD on InGaP/GaAs using an *in-situ* non-halogen, non-PH_3 dry-clean pre-treatment.

2. Experimental methods

The tri-ethylgallium (TEGa) and tri-*tert*-butylphosphine (tri-TBP, $(tert–C_4H_9)_3–P$, CAS number 13716-12-6) were provided by EMD Performance Materials and Strem Chemicals, respectively. Substrates of 6 mm × 12 mm were diced from a 100 mm wafer consisting of 15°-miscut InGaP MOCVD grown on GaAs. The composition of $In_{0.5}Ga_{0.5}P$ is expected by wafer production and in good agreement with our EDS result during cross-sectional STEM analysis. ACS Regent grade acetone (99.5+ wt.%), isopropyl alcohol (99.5+ wt.%), deionized (DI) water (99.5+ wt. %), and hydrofluoric (HF) acid (48 wt%) were purchased from Fisher Scientific. Ultra-high purity (UHP) grade Ar (99.999 vol%) and H_2 (99.999 vol%) were purchased from Praxair and purified using an Entegris Gatekeeper gas purifier for use as a purge gas for the ALD process.

Pre-diced InGaP/GaAs substrates were degreased by rinsing with acetone, isopropyl alcohol, and DI water, sequentially. On a subset of samples, mesa patterning was performed using a SiO_2 hard mask, lithographic patterning, and ICP dry-etching. The degreased substrates were loaded onto the isolated loading chamber, the chamber was pumped down to a pressure below 2×10^{-6} Torr, and the substrates were transferred to the ALD process chamber with a base pressure below 2×10^{-6} Torr. The native oxide was removed by *in-situ* dry-clean with tri-TBP pulses during continuous plasma with 75 W using 40 mTorr of Ar and 160 mTorr of H_2 without stage DC bias.

The commercial dry pump (Edwards EPX-500NE) pumped the customized ALD process chamber. The impurities, excess precursors, particulates, and moisture were collected by using a liquid nitrogen cold trap and stainless-steel mesh between the ALD process chamber and the dry pump. The ALD process was performed at 90 °C chamber wall temperature. Pneumatically actuated diaphragm ALD valves were installed and tri-TBP was dosed at 60 °C bottle temperature without push gas. The process temperature was measured by a direct contact thermocouple on the sample stage which was made of an electrically isolated copper block heated by a cartridge heater. The temperature of the sample stage was calibrated with the temperature of the thin copper sample holder to fix the sample prior to the ALD process with Ar gas at process pressure (10 mTorr–200 mTorr). Multiple doses of tri-TBP were employed to deliver a larger amount of precursor rather than a single dose of long pulse length to limit the maximum pressure on the drag pump. The RF remote plasma source (PIE Scientific) with a sapphire plasma tube was mounted above the chamber. Note the gases continue to flow through the plasma source when the plasma is not ignited thereby acting as a typical ALD purge gas. The atomic H plasma used a 15 s plasma treatment each cycle at a power of 75 W using 10 mTorr of Ar and 40 mTorr of H_2 without stage DC bias.

Chemical compositions were estimated by *in-situ* auger electron spectroscopy (AES) using a micro-cylindrical mirror Auger spectrometer (micro CMA, RBD Instruments). The as-deposited samples were transported *in-vacuo* to an attached AES chamber (base pressure below 1×10^{-8} Torr). The microCMA auger spectrometer scanned a kinetic energy range of 40–1500 eV with a step size of 1 eV. The beam potential was 3 kV with a filament current of 0.88 A. The AES results were collected and processed using CMapp software (RBD Instruments).

TEM analysis was performed on a Thermo-Fisher (FEI) Talos F200X G2 with a bright XFEG source and a high angle annular dark field (HAADF) detector. Energy dispersive X-ray spectroscopy (EDS) was measured on a Thermo-Fisher (FEI) Super X EDS detector during their HAADF-STEM analysis. The chemical compositions were estimated by converting EDS counts with Velox software. Selected area electron digital diffraction patterns were determined by using Gatan Microscopy Suites (GMS) software. The EAG Laboratories prepared the lamella for the cross-sectional TEM analysis using Thermo-Fisher (FEI) Helios UC FIB-SEM.

Top-view scanning electron microscopy (SEM) images were collected using a FEI Apreo scanning electron microscope at 5 kV electron voltage and 0.1 nA emission current. Atomic force microscopy (AFM) images with tapping mode were collected using Veeco Scanning Probe Microscope (Veeco Instruments, Woodbury, NY, USA) to investigate the surface morphology. Images and root mean square (RMS) surface roughness were analyzed using Gwyddion 2.60 scanning probe microscope (SPM) software with 5 μm × 5 μm of AFM images.

Ex-situ high-resolution X-ray photoelectron spectroscopy (XPS) was acquired on the as-deposited samples without any surface treatment (e.

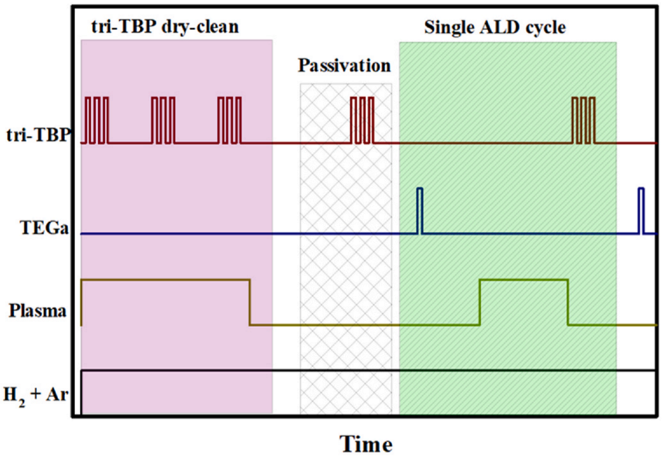

Fig. 1. Process parameters switching diagram for the *in-situ* tri-TBP dry-clean pre-treatment and GaP atomic H ALD process. The intensity of the y-axis illustrates pulse on/off switching regardless of pressure, the time of the x-axis displays only sequence and does not represent the specific pulse length.

g., Ar sputtering or UHV annealing) using a Mg Kα source and DESA 150 electron analyzer (Staib Instruments) at a collection angle of 45° relative to the surface normal using a step width of 0.1 eV (base pressure 5 × 10^{-10} Torr). The analyzed area was assumed to be less than 0.2 mm^2. Charge neutralization was not used in this study. The samples were transferred from the ALD process chamber to the XPS analysis chamber within 10 min. The binding energy (BE) of XPS was referenced by aligning the adventitious C 1s spectra (284.5 eV). The BE of adventitious C 1s was estimated by the work function method [29] and the previously reported work function of GaP films was used [30]. Analysis of the XPS data was performed in CasaXPS v2.3 using Shirley background subtraction and Scofield photoionization cross-sectional relative sensitivity factors.

3. Results and discussion

Fig. 1 shows the sequence of the process parameters switching during the *in-situ* tri-TBP dry-clean and GaP atomic H ALD growth process on InGaP/GaAs. The stage temperature of ALD chamber was increased up to target temperature under ultra-high vacuum pressure for 40 min. The 75 W remote RF plasma was employed for *n* min dry-clean with 50 or 200 mTorr of gas mixture (Ar : H_2 = 1 : 4) as shown in Fig. 1. During *n* min of the tri-TBP dry-clean pre-treatment step, six cycles of tri-TBP pulses (3 × 800 ms + 5 s purge) per minute were introduced into the ALD chamber; note the plasma is on during these pulses so there may be gas phase reactions between the atomic H and tri-TBP. Triple doses of tri-TBP were employed to deliver a larger amount of precursor than a single dose of long pulse length. After tri-TBP dry-clean, 3 × 800 ms of tri-TBP were dosed without plasma ignition to passivate the InGaP surface with phosphide functional groups. The ALD process cycles began on the functionalized InGaP surface with 10 mTorr of Ar and 40 mTorr of H_2. 200 ms of TEGa was dosed as a first ALD pulse with 10 s purge, 15 s of atomic H plasma was employed as a second ALD pulse without precursor dosing, and 3 × 800 ms of tri-TBP was dosed as a third ALD pulse with 10 s purge. Note in the ALD process, the plasma is off when the tri-TBP and TEGa are dosed.

The *ex-situ* AFM images of tri-TBP dry-cleaned InGaP/GaAs in 10 mTorr Ar and 40 mTorr H_2 as a function of the dry-clean time are shown in Fig. 2. Smooth surface morphologies (RMS = 0.4–2.7 nm) were observed with 0–5 min dry-clean on InGaP/GaAs, while the 5 μm × 5 μm AFM image of degrease only InGaP/GaAs (0 min dry-clean) was collected in a selected region without particles despite surface particles were widely observed in the degreased InGaP/GaAs (Fig. S1). Decreased O content and particles after dry-clean (1 min tri-TBP dry-clean in 50 mTorr) were observed by *in-situ* AES and *ex-situ* SEM top-view imaging (Figs. S2a and S2b, respectively), suggesting the removal of native oxide and surface particles. The surface roughness (RMS) gradually increased with the dry-clean time. The 5 min dry-cleaned InGaP/GaAs substrate showed a higher RMS value (2.7 nm) and different texture (Figure S2c and Fig. 2d) as compared to InGaP/GaAs with shorter than 3 min dry-clean. In addition, the formation of particles and pits with 2–5 μm diameters was observed in the SEM image of InGaP/GaAs with 10 min dry-clean (Fig. S2d). The statistical analysis for surface particles on InGaP/GaAs substrates after tri-TBP dry-clean as a function of plasma time and for two InGaP/GaAs substrates after wet-clean methods is shown in supporting information. The density of particles per 1000 μm^2 was estimated by counting particles (larger than 0.1 μm radius) in three different SEM top-view images of each sample. These observations indicated that the tri-TBP dry-clean not only removed the surface particles but also damaged the InGaP surface layer due to atomic H etching, which could have a detrimental impact on the formation of defects on the interface layer between InGaP substrate and GaP thin films. The etching impact of atomic H plasma could be minimized by increasing chamber pressure since the plasma ion current of atomic H should be decreased in high chamber pressure. The highly energetic Ar^+ and H^+ ions could be responsible for the atomic H plasma etching. It is previously reported that the relative ion concentrations of Ar^+ and H^+ at high pressure (48 mTorr H_2 + 12 mTorr Ar) were significantly lower than that in low pressure (8 mTorr H_2 + 2 mTorr Ar) [31] consistent with a mean free path being larger than the plasma to sample distance only at pressures below 10 mTorr. Note at high pressures (≥50 mtorr), no ions are expected to impact the surface; therefore, the active species from the plasma are assumed to be just atomic H.

For high pressure dry-clean, both the oxygen removal and surface roughness were quantified. The oxygen impurity content in InGaP/GaAs with dry-clean in 200 mTorr (40 mTorr Ar and 160 mTorr H_2) was decreased from ~26 at.% (degreased InGaP/GaAs) to 2.3 at.% (3 min dry-clean) as observed by *in-situ* AES (Fig. 3a). This suggested that *in-situ* tri-TBP dry-clean could remove the native oxide of InGaP/GaAs substrate from air exposure. Fig. 3b shows that the RMS surface roughness of 3 min tri-TBP dry-cleaned InGaP/GaAs in 40 mTorr Ar and 160 mTorr H_2 was similar to that of degreased InGaP/GaAs and nearly unchanged up to 5 min of dry-clean in 200 mTorr (RMS = 0.3–0.6 nm, Fig. S3). Furthermore, the RMS surface roughness of 3 min tri-TBP dry-clean in 200 mTorr (0.3 nm, Fig. 3b) was significantly lower than that in 50 mTorr (RMS surface roughness = 1.2 nm, Fig. 2c), suggesting that the dry-clean in high chamber pressure mitigated the detrimental etching of atomic H plasma. Particle-free InGaP/GaAs substrates were observed in the *ex-situ* SEM top-view images of InGaP/GaAs with longer than 2 min dry-clean in 200 mTorr (Fig. S4) with the absence of particles or pits. The *ex-situ* SEM, AFM images, and *in-situ* AES of tri-TBP dry-cleaned InGaP/GaAs in 40 mTorr of Ar and 160 mTorr H_2 suggested that surface particles and native oxide were effectively removed during dry-clean without significant etching damage of atomic H. The *in-situ* tri-TBP dry-clean in high pressure could preferentially facilitate the gas-phase reactions between tri-TBP and atomic H rather than the direct reactions of tri-TBP and atomic H on the InGaP surface since the mean free path of process gas (~1 mm) in 200 mTorr is one to two orders of magnitude smaller than the size of ALD chamber (~40 mm) and the distance between plasma source to sample (~100 mm). The cross-sectional TEM images of the interfacial region between GaP atomic H ALD thin films and *in-situ* tri-TBP dry-cleaned InGaP/GaAs are discussed further below.

The newly proposed *in-situ* tri-TBP dry-clean pre-treatment mechanism and previously proposed mechanism for GaP atomic H ALD [22] are shown in Fig. 4. After the wet-clean preparation step (degrease only) of the InGaP/GaAs substrate, a significant number of surface particles and native oxide layer (~26 at.% of oxygen) were observed in the *ex-situ* SEM (Fig. S1) and *in-situ* AES (Fig. 3a), respectively. The surface

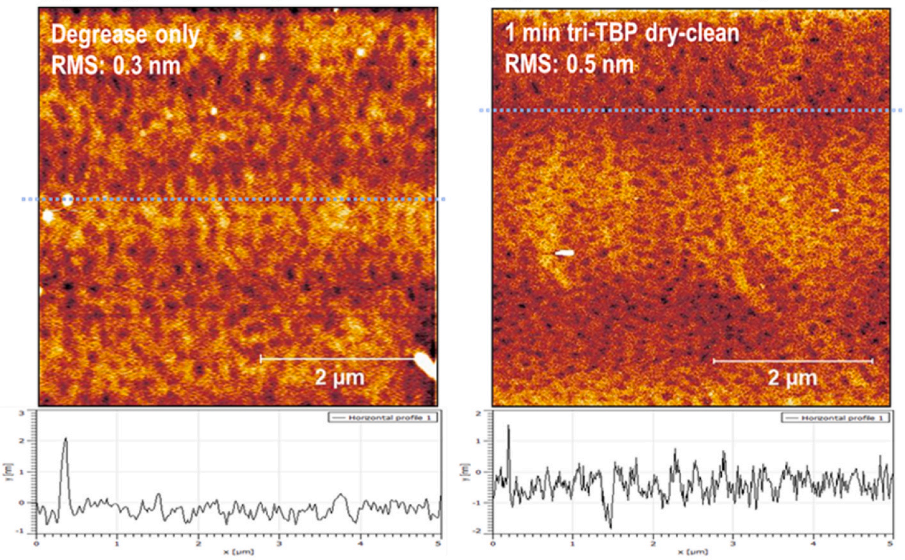
(a) Degrease only

(b) 1 min tri-TBP dry-clean

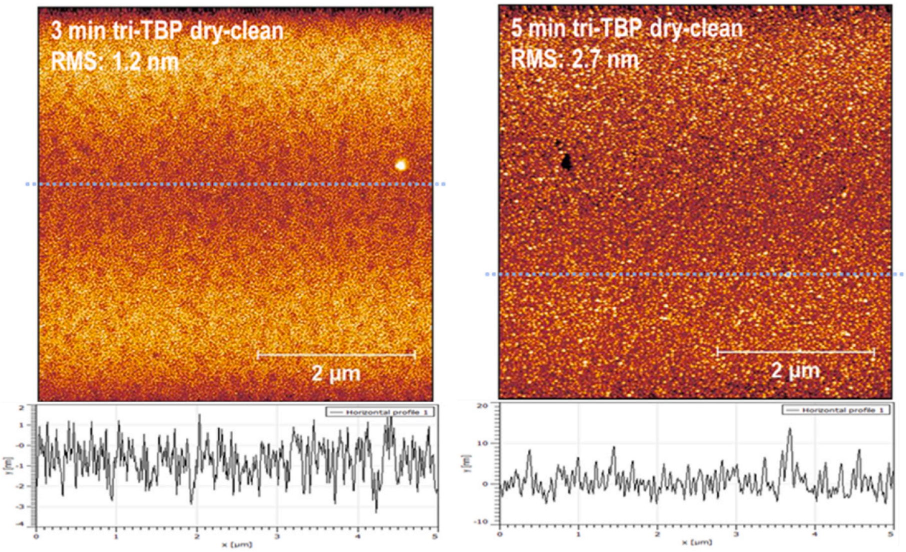
(c) 3 min tri-TBP dry-clean

(d) 5min tri-TBP dry-clean

Fig. 2. ***Ex-situ*** **AFM images and root mean square (RMS) roughness as a function of plasma time (0–5 min) for tri-TBP dry-cleaned InGaP/GaAs without GaP ALD process in 40 mTorr H_2 and 10 mTorr Ar.** Tri-TBP dry-clean: six cycles of tri-TBP pulses (3 × 800 ms tri-TBP + 5 s purge) per 1 min dry-clean with continuous 75 W plasma in 10 mTorr Ar + 40 mTorr H_2 at 500 °C samples temperature.

particles might mostly consist of Ga_2O_3 or In_2O_3 or As_2O_3 (hereafter M_2O_3, M = Ga or In or As) due to debris of the InGaP/GaAs wafer production/dicing process. As_2O_3 may also come from the degreased backside of the substrate. The M_2O_3 might be reduced to M_2O by atomic H and molecular hydrogen thermal deoxidation at 500 °C through the following reaction [23,24];

Atomic H plasma reduction: $M_2O_3(s) + 4H^0(g) \rightarrow M_2O(s) + 2H_2O(g)\uparrow$

H_2 thermal deoxidation: $M_2O_3(s) + 2H_2(g) \rightarrow M_2O(s) + 2H_2O(g)\uparrow$

It is assumed that the first process is more efficient since the plasma was required for the dry-clean pre-treatment method. The resulting M_2O could be vaporized at 500 °C since the partially reduced M_2O is more volatile than fully oxidized M_2O_3 [25,26]. It is known that atomic H can reduce the native oxide layer of InGaP (200) from Ga–O (In–O) to elemental Ga (In) [27] or Ga–H (In–H). At the same time, the reduced surface layer of InGaP could be functionalized to In- or Ga-PH_2 by reaction with $PH_x(C_4H_9)_y$, which was generated during tri-TBP dry-clean at 500 °C. Tri-TBP could undergo stepwise elimination of $CH_2{=}C(CH_3)_2$ [32]. The surface nucleation reaction would be thermodynamically favorable since the pKa of PH_3 is 27 and the pKa of H_2 is 35 [22]. The InGaP/GaAs surface would be fully passivated with P–H since the abundant atomic H is the final step of the dry-clean procedure. The tri-TBP dry-clean pre-treatment is illustrated with orange arrows in Fig. 4. The increased phosphorus content and decreased oxygen content in *in-situ* AES (Fig. 3a) after pre-treatment indicated that *in-situ* tri-TBP dry-clean could remove the native oxide and nucleate the InGaP surface simultaneously.

The mechanism of the GaP atomic H ALD process was previously proposed [22]. 3 × 800 ms of tri-TBP was introduced after *in-situ* tri-TBP dry-clean pre-treatment to fully functionalize the InGaP surface with the phosphide functional group. The first ALD pulse was injected with a single 200 ms of TEGa pulse after 10 s of purge time. The thermal decomposition of TEGa precursor above 350 °C was previously reported [33]. It is hypothesized that the partially decomposed $GaH_x(C_2H_5)_y$ could react with P–H sites of the functionalized InGaP surface. The 15 s

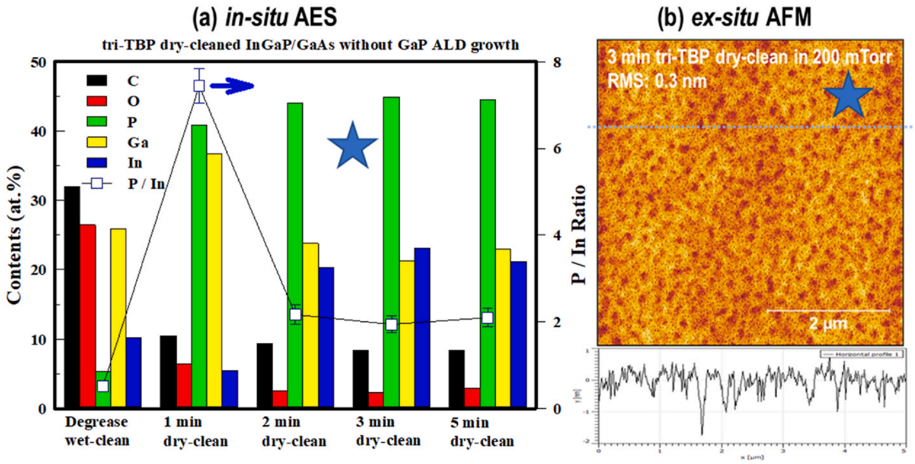

Fig. 3. Chemical compositions and surface morphology of tri-TBP dry-cleaned InGaP/GaAs in high chamber pressure (200 mtorr). Tri-TBP dry-clean: six cycles of tri-TBP pulses (3 × 800 ms of tri-TBP + 5 s purge) per 1 min dry-clean with continuous 75 W plasma in 40 mTorr Ar + 160 mTorr H_2 at 500 °C samples temperature. Low oxygen contents and stoichiometric P/In ratio in the *in-situ* AES of InGaP/GaAs with tri-TBP dry-clean time longer than 2 min (a) and smooth surface morphologies (RMS surface roughness = 0.3 nm) similar to bare InGaP/GaAs substrate (RMS = 0.3 nm) in AFM image of 3 min tri-TBP dry-cleaned InGaP/GaAs (b).

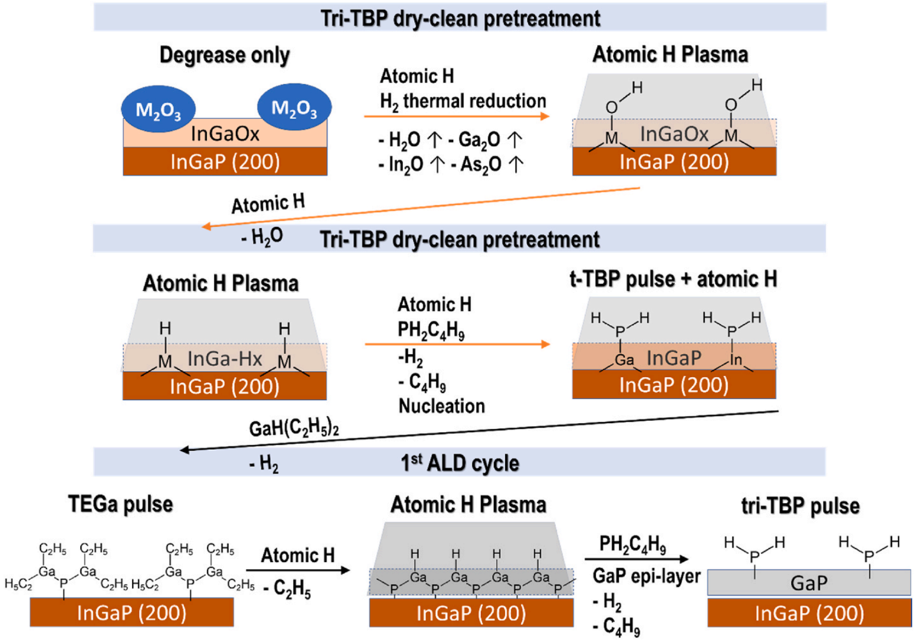

Fig. 4. Proposed mechanism of *in-situ* tri-TBP dry-clean pre-treatment and GaP atomic H ALD growth on degreased InGaP/GaAs. The proposed pre-treatment mechanism for the simultaneous removal of surface particles, removal of native oxide, and phosphide functionalization on InGaP (200) substrate using tri-TBP dry-clean, and growth mechanism of GaP atomic H ALD.

of atomic H plasma was introduced as the second ALD pulse after 10 s of purge time. It is proposed that the atomic H plasma could effectively remove the organic ligands (-C_2H_5 and –C_4H_9) and induce the formation of Ga–P thin films. Deminskyi et al. recently reported that the hydrogen plasma was able to remove the organic ligands of TEGa [34]. The mean free path of process gas at 50 mTorr is ~4 mm at 500 °C. It is hypothesized that at this pressure, the optimal amount of atomic H could travel randomly and react with surface -$PGa_2(C_2H_5)_4$ to remove organic ligands without ion-surface bombardment. By limiting the flux of plasma-stimulated H^+ and Ar^+ that directly impact the surface, etching is suppressed [22]. The optimal gas-phase surface reaction of atomic H could enable conformal deposition on the high aspect ratio structure. In addition to the removal of organic ligands, it is hypothesized that the remaining P–H bonds and Ga–H bonds could be deprotonated by atomic H and converted to the ordered Ga–P thin films. The topmost dangling bonds might be terminated by Ga–H bonds due to the abundant H_2 purge gas and the short interval (1 s) between the second atomic H plasma pulse and the third tri-TBP pulse. Lastly, the third ALD pulse was dosed with 3 × 800 ms of tri-TBP. It is proposed that the partially decomposed $PH_x(C_4H_9)_y$ from tri-TBP at 500 °C [32] could react with the Ga–H terminating sites of the as-deposited Ga–P thin films, converting to the Ga-PH_2 layer. The next TEGa pulse (the first ALD pulse of the next ALD cycle) could react with the functionalized P–H sites. The ALD cycles are illustrated with black arrows in Fig. 4.

Fig. 5 shows the chemical compositions of the GaP atomic H ALD on InGaP/GaAs as a function of process temperature using *in-situ* AES. The P/Ga atomic ratios were nearly stoichiometric ratio (P/Ga = 1.05) after 40 cycles of GaP atomic H ALD, suggesting the deposition of a high-

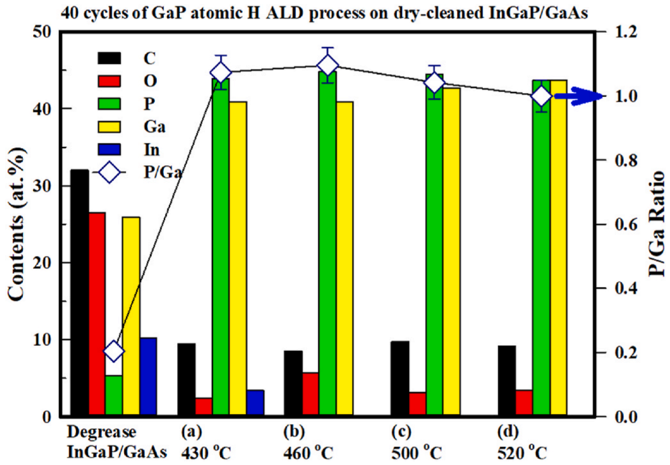

Fig. 5. ***In-situ* AES of GaP atomic H ALD on tri-TBP dry-cleaned InGaP/GaAs.** Chemical compositions over the as-deposited GaP atomic H ALD on InGaP/GaAs as a function of process temperature. 40 cycles of GaP atomic H ALD process in 10 mTorr Ar + 40 mTorr H_2, 200 ms of TEGa, 10 s purge, and 15 s of atomic H plasma pulse, 3 × 800 ms of tri-TBP, and 10 s purge.

quality GaP thin film on the InGaP substrate. The In signal from the substrate in the GaP atomic H ALD at 430 °C indicated extremely low growth of GaP layers and insufficient thermal energy to react two ligands of TEGa and tri-TBP on the InGaP surface at 430 °C, which agreed with previously reported GaP atomic H ALD deposition on Si substrate [22]. Oxygen content in GaP atomic H ALD at 460 °C was higher than GaP ALD films at other process temperatures which suggested optimal process temperature is needed for the formation of ordered GaP. The oxygen impurity in the GaP thin films could mostly come from the impurities of precursors and Ar purge gas. The atomic H plasma process might displace some oxygen from the chamber walls. The oxygen impurity contents of GaP atomic H ALD at 500 °C and 520 °C were lower than 3.1 at.%, which is nearly close to the noise signal of AES. Furthermore, the *ex-situ* AFM images of GaP atomic H ALD at 460 °C and 500 °C showed smooth surface morphology with less than 1.8 nm of RMS values (Fig. S5). The RMS surface roughness of GaP atomic H at 520 °C was increased to 3.0 nm, suggesting the aggregation of Ga–P due to solid diffusion during the ALD process at high temperature and a surface CVD process. The hazy and color-gradient GaP films on InGaP/GaAs were observed after the GaP atomic H ALD process at temperatures above 520 °C, consistent with a CVD process (not shown). These observations suggested that the ALD temperature window of the GaP atomic H ALD process on InGaP/GaAs is quite narrow within 460°C–500 °C, and 500 °C was chosen for optimal process temperature for GaP atomic H ALD on InGaP/GaAs.

Ex-situ XPS analysis revealed the presence of Ga–P bonds in the thin GaP films on InGaP/GaAs (Fig. 6). It is noted that no *in-situ* sputter clean was performed. The XPS survey scans for two different surface preparation techniques (tri-TBP dry-cleaned InGaP/GaAs and TEGa pre-pulsed InGaP/GaAs) are shown in Fig. S7a and have similar elements in the films without impurity elements and are in good agreement with literature survey scans [35]. The raw spectrum of C 1s and aligned spectrum of O1s are shown in Figs. S7b and S7c. The Ga $2p_{3/2}$ spectra of GaP atomic H ALD on *in-situ* tri-TBP dry-cleaned InGaP/GaAs and that of GaP atomic H ALD on TEGa pre-pulsed InGaP/GaAs with HF wet-clean are shown in Fig. 6a. The deconvoluted peaks at 1116.4 eV and 1117.8 eV were associated with the Ga–P and Ga–O species, respectively [35–37]. The binding energies of Ga–P species in both GaP atomic H ALD thin films are nearly identical, suggesting the presence of Ga–P bonds in both thin GaP films. Ga–O species in both films indicate the formation of native oxide on the top surface due to air exposure. The relative area ratio of Ga–P to Ga–O bonds in tri-TBP dry-cleaned InGaP/GaAs (2.2) was higher than that in TEGa pre-pulsed InGaP/GaAs (1.1) with HF wet-clean, suggesting the formation of ordered Ga–P thin films due to particle-free, oxide-free, and homogeneously nucleated InGaP surface with tri-TBP dry-clean as compared to that with HF wet-clean. The P 2p spectra of GaP atomic H ALD on tri-TBP dry-cleaned InGaP/GaAs and that of GaP atomic H ALD on TEGa pre-pulsed InGaP/GaAs with HF wet-clean are also shown in Fig. 6b. The dominant doublet at 128.7 eV corresponding to Ga–P was observed in both GaP atomic H ALD thin films [35–37] and insignificant doublets at 133.5–133.8 eV, suggesting that most P species in GaP thin films were not oxidized by air exposure and remained as Ga–P bonds during sample

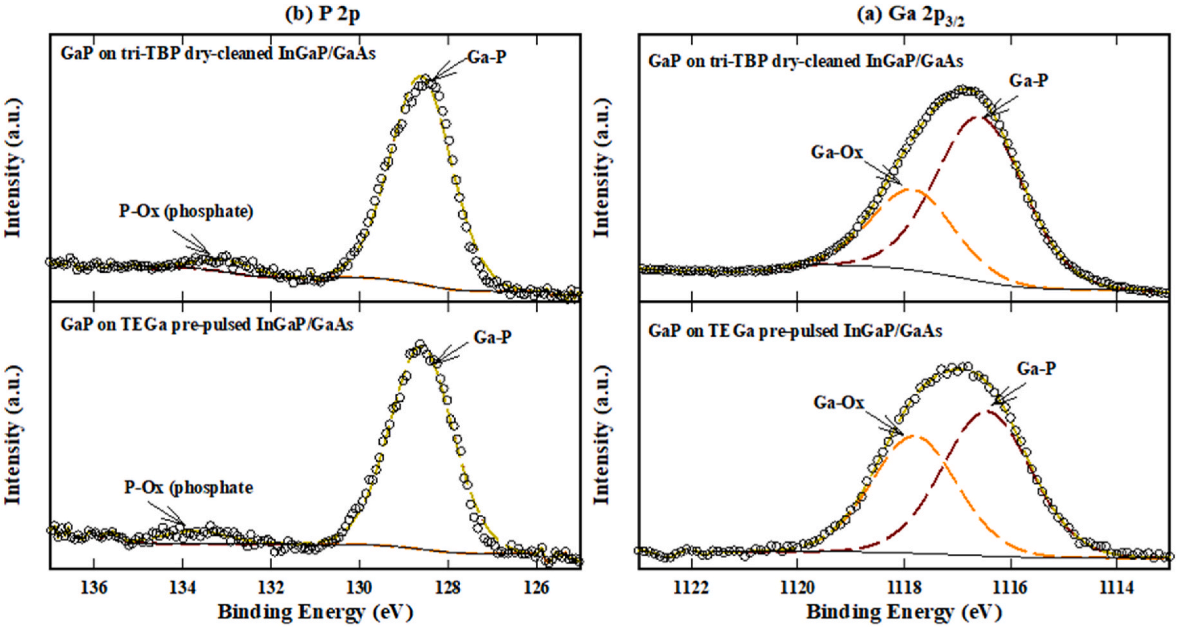

Fig. 6. ***Ex-Situ* XPS analysis of GaP/InGaP with two different surface preparation techniques. (a) Ga $2p_{3/2}$ region and (b) P 2p region for GaP thin films.** GaP atomic H ALD on tri-TBP dry-cleaned InGaP/GaAs and GaP atomic H ALD on TEGA pre-pulsed InGaP/GaAs with HF wet-clean were compared to confirm the presence of Ga–P bond and the formation of the ordered GaP. Note no *in-situ* sputter clean was performed so oxygen is from air exposure.

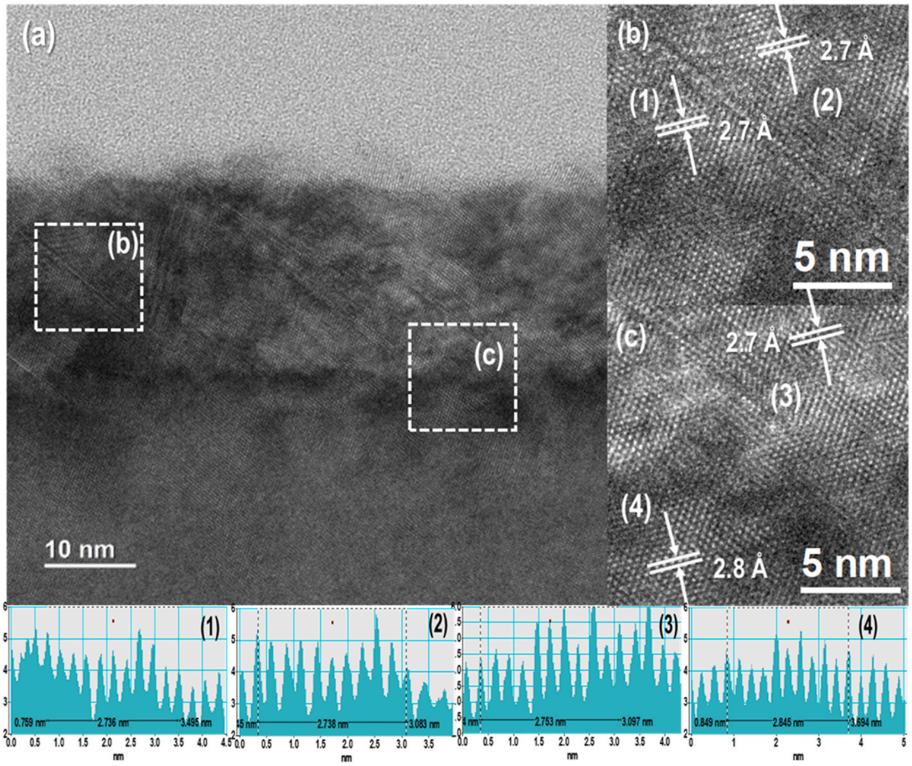

Fig. 7. HR-TEM images of (a–c) GaP atomic H ALD on *in-situ* tri-TBP dry-cleaned InGaP/GaAs. Local epitaxy growth of GaP (200) with lattice fringe (2.7 Å) was homogeneously on tri-TBP dry-cleaned InGaP (200) substrate with lattice fringe (2.8 Å) using atomic H ALD process.

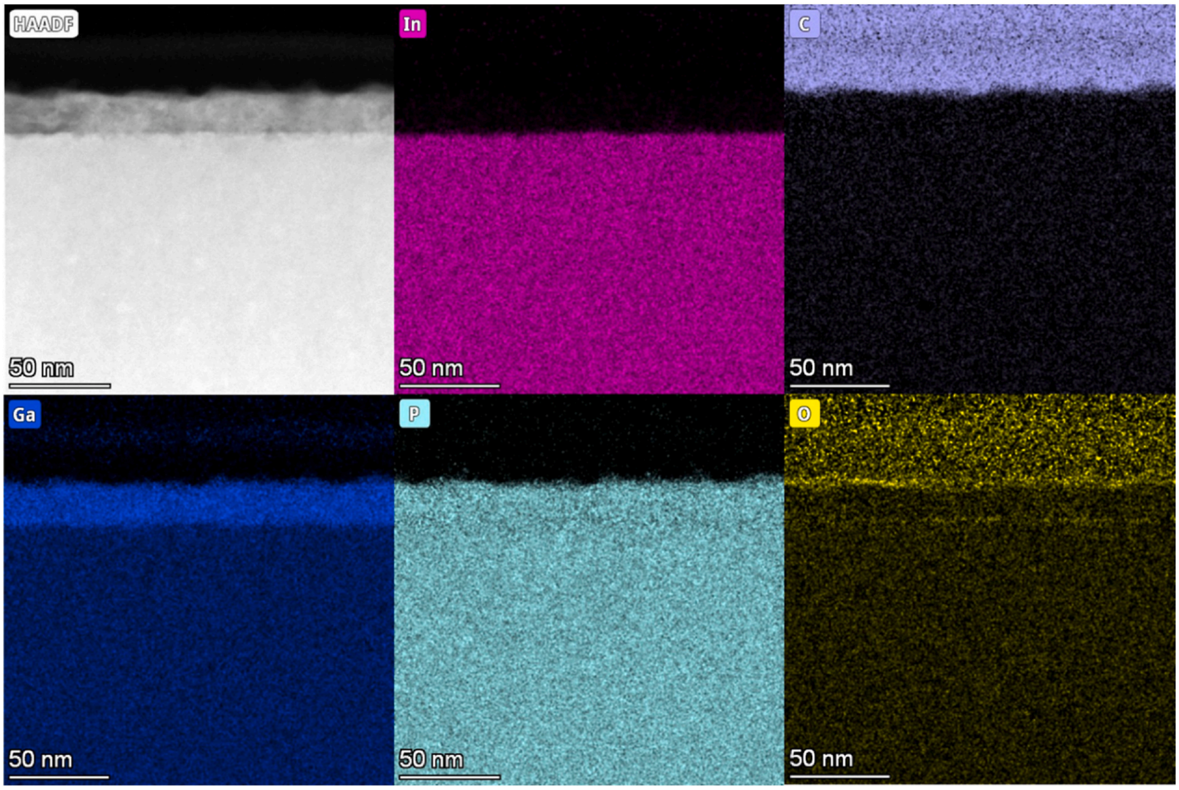

Fig. 8. HAADF-STEM image and EDS maps of (In, C, Ga, P, and O) of GaP Atomic H ALD on *in-situ* tri-TBP dry-cleaned InGaP/GaAs. Homogeneous GaP film growth with low oxygen content in the thin films, showing the formation of a high-quality interfacial layer without surface particles or impurities between InGaP surface and GaP thin films during *in-situ* tri-TBP dry-clean on InGaP/GaAs.

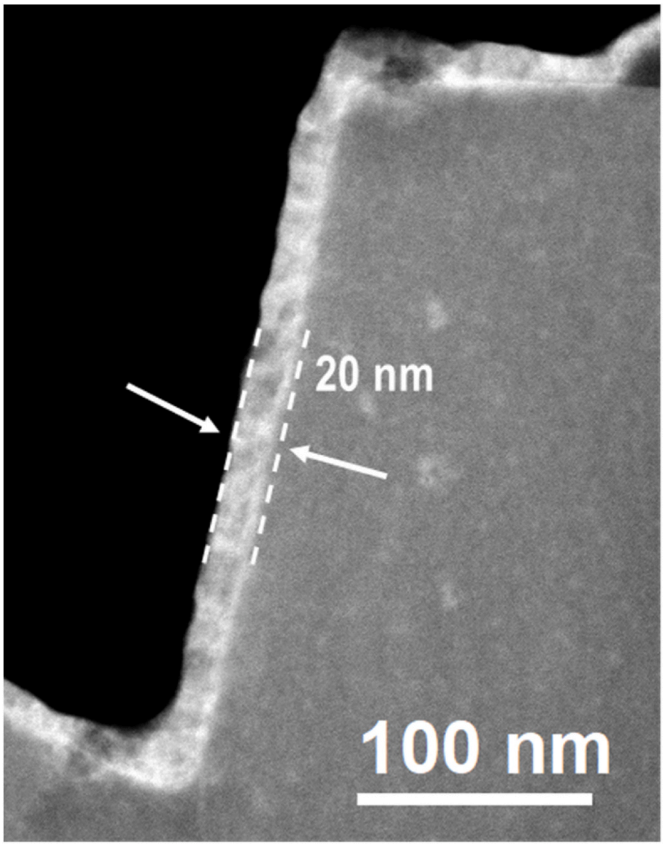

Fig. 9. STEM image of GaP atomic H ALD on *in-situ* dry-cleaned side-wall of InGaP layer. Conformal deposition of GaP atomic H ALD films on side-wall of InGaP layer with similar GPC to flat InGaP substrate, smooth surface morphology, and particle-free interfacial layer.

transfer.

Fig. 7 shows the HR-TEM images of cross-sectional GaP atomic H ALD thin films on tri-TBP dry-cleaned InGaP/GaAs. The distance of lattice fringes (1–4) in Fig. 7 of the selected areas was obtained by line-plots of HR-TEM images using Gatan Microscopy Suites (GMS) software. Fig. 7a–c show the presence of 2.7 Å and 2.8 Å lattice fringes, which correspond to the GaP (200) and InGaP (200) d-spacings, respectively. This suggested the local epitaxy growth of GaP thin films on *in-situ* tri-TBP dry-cleaned InGaP/GaAs. The insignificant contrast difference at the interface region between GaP thin films and InGaP substrate suggests a native oxide-free interface, particle-free interface, and the absence of metallic clusters during *in-situ* tri-TBP dry-clean.

HAADF-STEM image and corresponding EDS maps of indium, carbon, gallium, phosphorus, and oxygen over GaP atomic H ALD on *in-situ* tri-TBP dry-cleaned InGaP/GaAs are shown in Fig. 8. The uniform Z contrast of the GaP thin films was observed in the HAADF STEM image, indicating homogeneous GaP film growth on tri-TBP dry-cleaned InGaP/GaAs. The EDS map of oxygen shows extremely low oxygen impurity in the GaP thin films. In addition, the nearly invisible oxygen signal at the interfacial region in the EDS map of oxygen indicated that *in-situ* tri-TBP dry-clean effectively removed the native oxide of the InGaP substrate. The particle-free and impurity-free EDS maps at the interface between GaP thin films and InGaP substrate are consistent with the formation of a high-quality interfacial layer during the GaP atomic H ALD process on *in-situ* tri-TBP dry-cleaned InGaP/GaAs.

The cross-sectional STEM image (Fig. 9) of GaP thin films documents the conformal deposition of GaP atomic H ALD on the side-wall of InGaP layer. 20 nm of GaP thin films were uniformly deposited on ~600 nm of side-wall from bottom to top. The growth rate per cycle (GPC, 2.1 Å/cycle) of GaP thin films on the side-wall showed good agreement with the GPC (2.2 Å/cycle) of GaP thin films on flat InGaP/GaAs substrate. HAADF STEM images and selected area electron digital diffraction patterns of three regions of GaP Atomic H ALD on the InGaP side-wall revealed the local epitaxy growth of GaP thin films (Fig. 10). Fig. 10c shows that 2.88 Å and 2.93 Å lattice fringes corresponding to the GaP (200) and InGaP (200), respectively, are slightly larger than the reported 2.7 Å and 2.8 Å of GaP (200) and InGaP (200). This might be attributed to the variation of high-resolution STEM analysis during the drift-corrected-frame-integration process. However, a spacing of 2.8 Å between the diffraction pattern and center in the digital diffraction pattern was determined by GMS software in GaP thin films in good agreement with the (200) d-spacing of InGaP. 12 digital diffraction patterns (2 InGaP substrates, 3 interfacial regions, and 7 GaP thin films) in 5 nm × 5 nm of selected areas in three different HAADF STEM images showed essentially the same orientations of InGaP (200) and GaP (200) as shown in Fig. 10d–g, 10h-k, and 10l-o. These observations suggested the local epitaxy growth of GaP thin films on the side-wall of InGaP layer.

HAADF STEM image, EDS line profile, and EDS maps of P, Ga, In, and O over the GaP atomic H ALD on the side-wall of InGaP layer are shown in Fig. S6. The uniform Z contrast in the HAADF STEM image of GaP thin films indicated homogeneous deposition of GaP atomic H ALD on the side-wall of InGaP layer. 5–6 at.% of every element were estimated over the entire EDS line profile, which could result from the noise signal of EDS due to the instrumental error of EDS during high-resolution STEM analysis. Extremely low O impurity content and uniform chemical composition of Ga and P elements in GaP thin films indicated the formation of high P/Ga atomic ratio and low oxygen content GaP thin films. Furthermore, an insignificant amount of oxygen and other impurities at the interfacial layer between GaP thin films and InGaP layer is consistent with the *in-situ* tri-TBP dry-clean and GaP atomic H ALD being an effective pre-treatment and buffer layer for the integrated III-V semiconductor structures with high aspect ratio.

4. Conclusions

The 3 min dry-clean with tri-TBP pulses during 75 W plasma in 40 mTorr Ar and 160 mTorr H_2 removed effectively surface particles and native oxide of InGaP simultaneously. *Ex-situ* SEM and AFM images showed the nearly particle-free InGaP/GaAs surface without atomic H etching after 3 min tri-TBP dry-clean showing smooth surface morphology (RMS surface roughness = 0.3 nm) at 200 mTorr. STEM analysis, EDS maps, and *in-situ* AES of *in-situ* dry-cleaned InGaP/GaAs revealed nearly oxide-free (~2.3 at.%), impurity-free, and particle-free interfacial layer between GaP thin films and InGaP surface, which is desirable for minimizing interface defects. The data is consistent with atomic H reduction for surface native oxides followed by *in-situ* formation of $PH_x(C_4H_9)_y$ surface adsorbates from atomic H and tri-TBP surface reactions. The -PH_2 surface species create a surface which is sufficiently reactive for subsequently ALD with a low temperature organic phosphide based process.

Local epitaxy growth of GaP on InGaP/GaAs with a high P/Ga atomic ratio (P/Ga = 1.05), low O content (~3.1 at.%), and smooth surface morphology (RMS surface roughness = 1.6 nm) was achieved using an atomic H plasma ALD process by tuning the process temperature and by using *in-situ* tri-TBP dry-cleaned InGaP/GaAs substrate. Finally, ~20 nm high-quality (high P/Ga atomic ratio and low oxygen content) GaP thin films were successfully deposited on the side-wall of the InGaP layer with the particle-free and oxide-free interface which was confirmed by cross-sectional STEM images and EDS maps. The digital electron diffraction patterns of STEM images indicated local epitaxy growth of GaP (200) on InGaP (200). The 15 s atomic H pulses in 10 mTorr Ar and 40 mTorr H_2 could provide the optimal amount of gas-phase surface reaction of atomic H to remove the organic ligands on a high aspect ratio structure without etching, which led to the formation of the conformal ordered GaP thin films on side-wall of InGaP layer. A mechanism was proposed in which the *in-situ* tri-TBP dry-clean at high pressure could

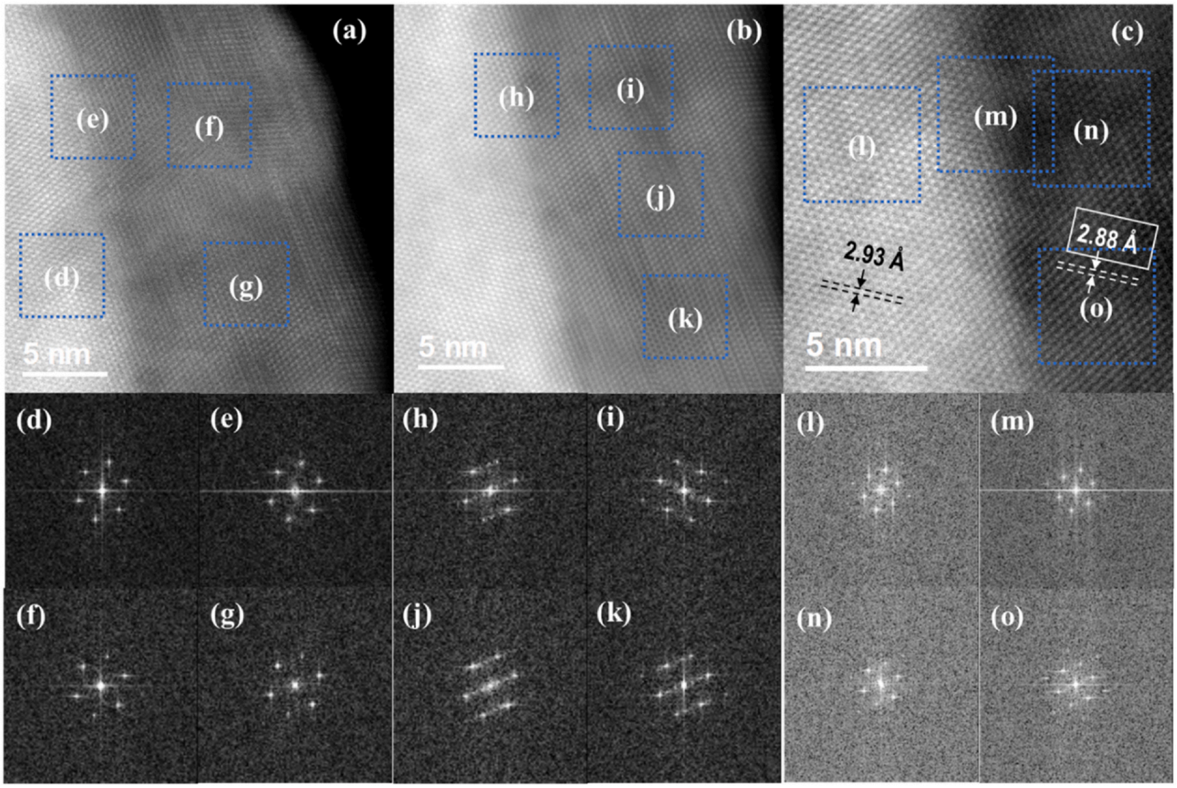

Fig. 10. HAADF-STEM images of (a–c) GaP atomic H ALD on tri-TBP dry-cleaned side-wall of InGaP layer and digital diffraction patterns using FFT of corresponding regions. Local epitaxy growth of GaP (200) with corresponding d-spacing and essentially same orientations (digital diffraction patterns) of InGaP (200) at tri-TBP dry-cleaned side-wall of InGaP layer.

remove the surface native oxide and nucleate the InGaP surface to -PH_2 functional group simultaneously. A high pressure (200 mTorr) during the dry-clean was proposed to promote the gas-phase surface reaction of tri-TBP and atomic H rather than H^+ or Ar^+ induced etching of the InGaP surface. The *in-situ* dry-clean without wet-etching is critical to the further development of in-line III-V semiconductor devices on high aspect ratio structures.

CRediT authorship contribution statement

SeongUk Yun: Writing – review & editing, Writing – original draft, Visualization, Validation, Resources, Methodology, Investigation, Formal analysis, Data curation, Conceptualization. **Ping-Che Lee:** Investigation, Formal analysis. **Cheng-Hsuan Kuo:** Investigation, Formal analysis. **Aaron J. Mcleod:** Investigation, Formal analysis. **Zichen Zhang:** Investigation. **Victor Wang:** Software, Methodology. **James Huang:** Methodology. **Harshil Kashyap:** Methodology. **Charles H. Winter:** Writing – review & editing, Validation, Methodology. **Andrew C. Kummel:** Writing – review & editing, Supervision, Project administration, Methodology, Funding acquisition, Conceptualization.

Declaration of competing interest

The authors declare the following financial interests/personal relationships which may be considered as potential competing interests:

Andrew C. Kummel reports financial support was provided by University of California San Diego.

Data availability

Data will be made available on request.

Acknowledgments

The authors gratefully acknowledge funding support from the UCSD Center for Memory and Recording Research.

Appendix A. Supplementary data

Supplementary data to this article can be found online at https://doi.org/10.1016/j.vacuum.2023.112806.

References

[1] J.A. del Alamo, Nature 479 (2011) 317–323.
[2] D.J. Wilson, K. Schneider, S. Hönl, M. Anderson, Y. Baumgartner, L. Czornomaz, T. J. Kippenberg, P. Seidler, Nat. Photonics 14 (2020) 57–62.
[3] S.M. George, Chem. Rev. 110 (2010) 111–131.
[4] S.F. Yoon, K.W. Mah, H.Q. Zheng, P.H. Zhang, J. Cryst. Growth 208 (2000) 197–204.
[5] A.C. Liu, K.J. Singh, Y.-M. Huang, T. Ahmed, F.-J. Liou, Y.-H. Liou, C.-C. Ting, C.-C. Lin, Y. Li, S. Samukawa, H.-C. Kuo, IEEE Nanotechnology Magazine 15 (2021) 18–34.
[6] L. Zhang, E.G. Wang, Q.K. Xue, S.B. Zhang, Z. Zhang, Phys. Rev. Lett. 97 (2006), 126103.
[7] M.S. Wong, D. Hwang, A.I. Alhassan, C. Lee, R. Ley, S. Nakamura, S.P. DenBaars, Opt Express 26 (2018) 21324–21331.
[8] J.K. Kim, S.I. Cho, S.H. Lee, C.K. Kim, K.S. Min, G.Y. Yeom, J. Vac. Sci. Technol. A 31 (2013), 061302.
[9] S.S. Han, A. Higo, W. Yunpeng, M. Deura, M. Sugiyama, Y. Nakano, S. Panyakeow, S. Ratanathammaphan, Microelectron. Eng. 112 (2013) 143–148.
[10] P. Xue, Y. Wang, E. Tikhonov, Comput. Mater. Sci. 209 (2022), 111351.
[11] Y. Sakuma, K. Kodama, M. Ozeki, Appl. Phys. Lett. 56 (1990) 827–829.
[12] K. Momose, H. Yonezu, Y. Fujimoto, Y. Furukawa, Y. Motomura, K. Aiki, Appl. Phys. Lett. 79 (2001) 4151–4153.
[13] S. Murali, N.P. Irvin, C. Zhang, R.R. King, C.B. Honsberg, *IEEE 46th Photovoltaic Specialists Conference (PVSC)* **2019**, 2019, pp. 1044–1048.
[14] M. Sadeghi, S. Wang, J. Cryst. Growth 227–228 (2001) 279–283.
[15] C. Zhang, N.N. Faleev, L. Ding, M. Boccard, M. Bertoni, Z. Holman, R.R. King, C. B. Honsberg, *IEEE 43rd Photovoltaic Specialists Conference (PVSC)* **2016**, 2016, pp. 1950–1953.

[16] J.M. Olson, A. Kibbler, J. Cryst. Growth 77 (1986) 182–187.
[17] M. Feifel, J. Ohlmann, J. Benick, T. Rachow, S. Janz, M. Hermle, F. Dimroth, J. Belz, A. Beyer, K. Volz, D. Lackner, IEEE J. Photovoltaics 7 (2017) 502–507.
[18] R. Cariou, W. Chen, J. Maurice, J. Yu, G. Patriarche, O. Mauguin, L. Largeau, J. Decobert, P. Roca i Cabarrocas, Sci. Rep. 6 (2016), 25674.
[19] H.C.M. Knoops, T. Faraz, K. Arts, W.M.M. Kessels, J. Vac. Sci. Technol. A 37 (2019), 030902.
[20] A.S. Gudovskikh, A.V. Uvarov, I.A. Morozov, A.I. Baranov, D.A. Kudryashov, E. V. Nikitina, A.A. Bukatin, K.S. Zelentsov, I.S. Mukhin, A. Levtchenko, S. Le Gall, J. Kleider, J. Renew. Sustain. Energy 10 (2018), 021001.
[21] A.V. Uvarov, A.S. Gudovskikh, V.N. Nevedomskiy, A.I. Baranov, D.A. Kudryashov, I.A. Morozov, J. Kleider, J. Phys. D 53 (2020), 345105.
[22] S. Yun, C. Kuo, P. Lee, S.T. Ueda, V. Wang, H. Kashyap, A.J. Mcleod, Z. Zhang, C. H. Winter, A.C. Kummel, Appl. Surf. Sci. 619 (2023), 156727.
[23] M. Yamada, Y. Ide, K. Tone, Appl. Surf. Sci. 70–71 (1993) 531–535.
[24] E. Weiss, O. Klin, S. Grossman, S. Greenberg, P.C. Klipstein, R. Akhvlediani, R. Tessler, R. Edrei, A. Hoffman, J. Vac. Sci. Technol. A 25 (2007) 736–745.
[25] Z. Lu, Y. Jiang, W.I. Wang, M.C. Teich, R.M. Osgood, J. Vac. Sci. Technol. B: Microelectronics and Nanometer Structures Processing, Measurement, and Phenomena 10 (1992) 1856–1861.
[26] N. Razek, K. Otte, T. Chassé, D. Hirsch, A. Schindler, F. Frost, B. Rauschenbach, J. Vac. Sci. Technol. A 20 (2002) 1492–1497.
[27] E. R. Cleveland, L. B. Ruppalt, B. R. Bennett, S. M. Prokes, Appl. Surf. Sci., 10.1016/j.apsusc.2013.04.018..
[28] S. Klejna, S.D. Elliott, J. Phys. Chem. C 116 (2012) 643–654.
[29] G. Greczynski, L. Hultman, Appl. Surf. Sci. 451 (2018) 99–103.
[30] M.V. Lebedev, P.A. Dementev, T.V. Lvova, V.L. Berkovits, Journal of materials chemistry. C, Materials for optical and electronic devices 7 (2019) 7327–7335.
[31] M. Jiménez-Redondo, M. Cueto, J.L. Doménech, I. Tanarro, V.J. Herrero, RSC Adv. 4 (2014) 62030–62041.
[32] G. Kaneda, J. Murata, T. Takeuchi, Y. Suzuki, N. Sanada, Y. Fukuda, Appl. Surf. Sci. 113–114 (1997) 546–550.
[33] J.A. McCaulley, R.J. Shul, V.M. Donnelly, J. Vac. Sci. Technol. A 9 (1991) 2872–2886.
[34] P. Deminskyi, C. Hsu, B. Bakhit, P. Rouf, H. Pedersen, J. Vac. Sci. Technol. A 39 (2021), 012411.
[35] B. Tilmann, G. Grinblat, R. Berté, M. Özcan, V.F. Kunzelmann, B. Nickel, I.D. Sharp, E. Cortés, S.A. Maier, Y. Li, Nanoscale horizons 5 (2020) 15–158.
[36] X. Zhang, S. Ptasinska, Phys. Chem. Chem. Phys. : Phys. Chem. Chem. Phys. 59 (2016) 564–573.
[37] V.I. Nefedov, Y.V. Salyn, E.P. Domashevskaya, Y.A. Ugai, V.A. Terekhov, J. Electron. Spectrosc. Relat. Phenom. 6 (1975) 231.